



## Collapse dynamics and deposition morphology of low-viscocohesive granular columns on a rough horizontal surface

Thanh-Trung Vo <sup>1,2,\*</sup> and Trung-Kien Nguyen <sup>3</sup>

<sup>1</sup>*School of Transportation Engineering, Danang Architecture University, 566 Nui Thanh St., Da Nang City, Vietnam*

<sup>2</sup>*Office of Research Administration, Danang Architecture University, 566 Nui Thanh St., Da Nang City, Vietnam*

<sup>3</sup>*Faculty of Building and Industrial Construction, Hanoi University of Civil Engineering, 55 Giai Phong Road, Hanoi, Vietnam*



(Received 11 November 2022; revised 5 September 2023; accepted 5 January 2024; published 24 January 2024)

Using the three-dimensional discrete element method, we numerically investigate the collapse dynamics and deposition morphology of low-viscocohesive granular columns on a rough-horizontal plane by systematically varying a broad range of values of the initial column aspect ratio, cohesive stress, and liquid viscosity. The results show that the kinetic energy, half runout time, and runout distance increase with increasing the initial column aspect ratio but decrease with increasing the cohesive and viscous effects of the binding liquid, while the toe angle and deposit height decrease with increasing the aspect ratio and increase with increasing cohesive stress and liquid viscosity. Remarkably, by defining a dimensionless scaling number that incorporates the Bond number and initial column aspect ratio, this allows us to nicely describe the kinetic energy, half runout time, deposition height, runout distance, and toe angle. These unified descriptions may provide insights into the physical properties of the collapse dynamics and deposition morphology of low-viscocohesive granular columns, leading to good explanations of the complex properties of natural disaster events.

DOI: [10.1103/PhysRevE.109.014904](https://doi.org/10.1103/PhysRevE.109.014904)

### I. INTRODUCTION

Granular flows are commonly found in natural events (e.g., landslides, rock avalanches, snow avalanches, debris flows) [1–11] and industrial processes (e.g., additive manufacturing, mineral processing, food processing, pharmaceutical engineering, and civil engineering applications) [12–14]. In nature, the granular flows induced from such natural hazards with high destructive energy and runout distance may create a negative impact on construction and the environment and threaten human lives [15,16]. Understanding the complex mechanism of granular flows may lead to good prediction, effective risks assessment and mitigation of the natural disaster damage, and optimization of the industrial processes [17–19]. This context leads to increasing the preferred attention of research works on granular flows in different disciplines and configurations in science and engineering [14,20–27].

In a significant number of research works on the flows of the granular materials in both numerical simulations and experiments, the gravity-driven collapse of a granular column on a flat or rough horizontal plane has been preferably considered due to the representation of the potential links to several physical and mechanical properties of natural disaster events. A granular column is allowed to collapse by lifting, rotating, or immediately removing its gate or wall. The granular materials then flow down, heap, and spread for a long distance before reaching a deposit height and runout distance in the final stage, which mainly depends on the column size, raw material properties, and liquid properties. Due to the representation of a simple interaction law between nonwetted particles, most

previous works have been focused on the collapse behavior of dry granular columns. In dry granular materials, the collapse dynamics characterized by the runout distance and the deposition height were first experimentally investigated, and they are introduced as a function of the aspect ratio (the ratio of the initial height and initial width of a column) [28–30]. Various experimental and numerical works were then carried out to study the similar behavior of dry granular columns [31–37].

In the case of the fluid phase in granular materials, the cohesive and viscous forces between grains cannot be negligible when investigating the collapse dynamics and runout distance of granular column collapse [38–41]. In a pendular state, a capillary bond induces a tensile or compressive force depending on the relative displacement between grains. The tensile force has the direction of extension, while the compressive force occurs along the direction of contraction [42]. Besides the governing of the particle inertia as well as the frictional and collisional forces between grains on the physical and mechanical behavior of dry granular materials, the collapse and runout dynamics are strongly modified by the cohesive forces [40,43,44]. Indeed, the cohesive forces tend to reduce the runout distance [43] and may control the surface roughness of granular deposits [45]. Due to the compensation between the inertial effects and the viscous effects (known as contractive and extensive properties), the spreading velocity, runout distance, deposit morphology, transient behavior, dilatancy, and flow regimes for the case of granular materials immersed in a viscous fluid strongly differ with the dry case depending on the initial solid packing, particle size, and aspect ratio of the granular columns [46–57].

In general, the above observations have provided a fundamental understanding of the failure mechanism and collapse dynamics of granular columns for separately considering

\*trungvt@dau.edu.vn

different cases of granular materials (e.g., dry, cohesive, or immersed). However, the comprehensive understanding of the combined effects of the liquid properties and inertial effects of grains remains further limited. Although recent observations have provided unified descriptions of the physical and mechanical properties of granular materials and the material and system parameters in other configurations such as pressure-controlled shear flow [27], gravity-driven simple shear flow [26], the evolution of aggregates [58,59], and the dynamic impact of visco-cohesive aggregates [60], the collapse dynamics and deposition morphology of low-viscocohesive granular columns commonly found in nature (e.g., landslides, debris flows) are different and should be also fully investigated. Li *et al.* [61] experimentally described the deposit height, runout distance, and deposit area of unchanneled wet granular column collapse by defining a dimensionless number that incorporated the Bond number and water content, but the effects of the initial column aspect ratio and liquid viscosity were neglected. More recently, Wu *et al.* [62] numerically proposed scaling laws for the deposition morphology of the collapse of wet granular columns by using the dimensionless cohesion number, combining the Bond number and system size. Although the deposit height, runout distance, and surface roughness of the deposit are nicely scaled by this cohesion number, the effects of viscosity were not clarified as well as without considering the collapse mobilities of the column.

In this paper a comprehensive investigation of the effects of the initial column aspect ratio and liquid properties on the collapse dynamics and deposition morphology of a low-viscocohesive granular column by means of three-dimensional (3D) discrete element method (DEM) simulations is considered and reported. In the simulations, the interactions between particles are considered by integrating the frictional contact force laws and the inclusion of the capillary attraction force law enhanced by the cohesive forces and viscous forces between grains. The numerical model is prepared by using the periodic boundary conditions in the  $y$  direction and generated by immediately removing its front gate. By varying a broad range of values of the initial aspect ratio, cohesive stress between particles, and viscosity of the binding liquid, we comprehensively study the collapse dynamics characterized by the energy evolution and half runout time and the deposition morphology characterized by the deposit height, runout distance, and toe angle. As we shall see, the physical quantities such as the kinetic energy in the collapse and heap phase, half runout time, deposit height, runout distance, and toe angle are excellently described by a new dimensionless number that incorporates the Bond number and initial column aspect ratio, leading to providing evidence for describing complex properties of natural disaster events.

The rest of the paper is organized as follows: we introduce the numerical method and the model setting with principal parameters in Sec. II. The paper then analyzes the collapse dynamics and morphology evolution of low-viscocohesive granular columns in Sec. III. In Sec. IV we introduce unified correlations between the physical quantities and a new dimensionless number. We give further discussion and remarks in Sec. V and conclude with a summary of salient results in Sec. VI.

## II. NUMERICAL METHOD AND COLLAPSE MODEL SETTING

### A. Numerical method

The discrete element method (DEM) has been used for the simulations of granular materials in different configurations and environments in science and engineering [63,64]. In DEM, the requirement of a large repulsive stiffness and a high time resolution is considered to compute the interactions between particles. Each particle is modeled as a rigid body and interacts with its neighboring grains by integrating a contact force law which is characterized by the normal and tangential contact forces [64,65]. These forces are calculated based on the relative displacement between grains, and the movements of particles are determined by Newton's second law [64]. The equation of motion of a particle  $i$  with its radius  $R_i$  is obtained by integrating all forces exerted on particle  $i$ . In wet granular materials, these forces involve the normal contact forces  $f_n$ , the tangential forces  $f_t$ , the cohesive forces  $f_c$ , the viscous forces  $f_v$ , and the gravitational forces [60]. Thus, the equations of motion of a wetted particle  $i$  are given by the following expressions:

$$\begin{aligned} m_i \frac{d^2 \mathbf{r}_i}{dt^2} &= \sum_j [(f_n^{ij} + f_c^{ij} + f_v^{ij}) \mathbf{n}^{ij} \\ &\quad + (f_c^{ik} + f_v^{ik}) \mathbf{n}^{ik} + f_t^{ij} \mathbf{t}^{ij}] + m_i \mathbf{g}, \\ \mathbf{I}_i \frac{d\boldsymbol{\omega}_i}{dt} &= \sum_j f_t^{ij} \mathbf{c}^{ij} \times \mathbf{t}^{ij}, \end{aligned} \quad (1)$$

where particle  $i$  is contacting the particle  $j$  and noncontacting particle  $k$ .  $\boldsymbol{\omega}_i$  is the angular velocity vector of the particle  $i$ ,  $\mathbf{g}$  is the gravitational acceleration vector, and  $m_i$ ,  $\mathbf{I}_i$ , and  $\mathbf{r}_i$  denote the mass, inertia matrix, and position of particle  $i$ , respectively.  $\mathbf{n}^{ij}$  ( $\mathbf{n}^{ik}$ ) is the normal unit vector between particle  $i$  and particle  $j$  ( $k$ ), and pointing from particle  $j$  ( $k$ ) to particle  $i$ .  $\mathbf{t}^{ij}$  is the tangential unit vector when particle  $i$  in contacting particle  $j$ , and having the direction opposite to the relative tangential movement.  $\mathbf{c}^{ij}$  is the unit vector that points from the particle center  $i$  to the contact point with its neighboring particle  $j$ .

The normal contact force  $f_n$  between grains is given by

$$f_n = f_n^e + f_n^d, \quad (2)$$

$f_n^e = -k_n \delta_n$  is the normal elastic force, as a linear function of the normal elastic deflection  $\delta_n$  at the contact point, where  $k_n$  is the normal stiffness, and  $f_n^d = -\gamma_n \dot{\delta}_n$  is the normal damping forces and is proportional to the relative normal velocity  $\dot{\delta}_n$ , where  $\gamma_n$  is the normal viscous damping parameter. These contact forces occur only when having the overlap between particles ( $\delta_n < 0$ ).

$f_t$  is the tangential force, expressed as the sum of the tangential elastic force  $f_t^e = k_t \delta_t$  and a tangential damping force  $f_t^d = \gamma_t \dot{\delta}_t$ , where  $k_t$  denotes the tangential stiffness,  $\gamma_t$  is the tangential damping coefficient, and  $\delta_t$  and  $\dot{\delta}_t$  are the tangential movement and the tangential velocity, respectively. According to the Coulomb friction law [64,65], the frictional force is given by

$$f_t = -\min\{(k_t \delta_t + \gamma_t \dot{\delta}_t), \mu(f_n + f_c + f_v)\}. \quad (3)$$

In our simulations, the liquid is in the form of capillary bridges (a pendular regime), which are assumed to be distributed homogeneously inside a granular column [66,67]. Each capillary bridge commonly induces the cohesive force and viscous force up to the rupture distance. During the collapse process of granular materials, a capillary bridge can be broken when the separation distance between grains is beyond the rupture distance. After breaking, the liquid is assumed to recover the particle surface proportional to the size of the particles and reform when occurring contact between them. These assumptions have been proposed in previous works and provide an excellent agreement with experimental data as well as show consistent physical meanings [42,68].

The cohesive force  $f_c$  depends on the liquid volume  $V_b$  of the capillary bridge, liquid-vapor surface tension  $\gamma_s$ , and the solid-liquid-gas contact angle  $\theta$ , which is assumed to be zero due to the full covering of the liquid on the particle surface. This cohesive force is calculated from the Laplace-Young equation, and an approximate solution of this equation is given by [12]

$$f_c = \begin{cases} -\kappa R, & \text{for } \delta_n < 0, \\ -\kappa R e^{-\delta_n/\lambda}, & \text{for } 0 \leq \delta_n \leq d_{\text{rupt}}, \\ 0, & \text{for } \delta_n > d_{\text{rupt}}, \end{cases} \quad (4)$$

where  $R = \sqrt{R_i R_j}$  is the geometrical mean radius of two particles  $i$  and  $j$  in capillary contact, and  $\kappa$  is the capillary force prefactor:

$$\kappa = 2\pi\gamma_s \cos\theta. \quad (5)$$

In the pendular regime, a capillary bond may be broken when the separation distance exceeds the rupture distance  $d_{\text{rupt}}$ , obtained by [66]

$$d_{\text{rupt}} = \left(1 + \frac{\theta}{2}\right) V_b^{1/3}. \quad (6)$$

$\lambda$  is the fall-off characteristic in Eq. (5), given by

$$\lambda = c h(r) \left(\frac{V_b}{R'}\right)^{1/2}, \quad (7)$$

where  $R' = 2R_i R_j / (R_i + R_j)$  denotes the harmonic mean radius,  $r = \max\{R_i/R_j; R_j/R_i\}$  is the size ratio between two primary particles,  $h(r) = r^{-1/2}$ , and  $c \simeq 0.9$  [59,69].

In this work the volume of capillary bridges is assumed to be mainly accounted for by the rupture distance, implying without considering the liquid bridge cross section [27,59]. This assumption leads to the calculation of the normal viscous force  $f_v$  between two smooth spherical particles based on only the lubrication effect of liquid bridges, implying the viscous dissipation is totally arisen from the normal displacement [58,70,71],

$$f_v = \frac{3}{2}\pi R^2 \eta \frac{v_n}{\delta_n}, \quad (8)$$

where  $\eta$  is the liquid viscosity and  $v_n$  is the relative normal velocity. In order to prevent the divergence of the viscous force when the gap between particles tends to zero, we introduce a characteristic length  $\delta_{n0}$ , reflecting the depth of the particle

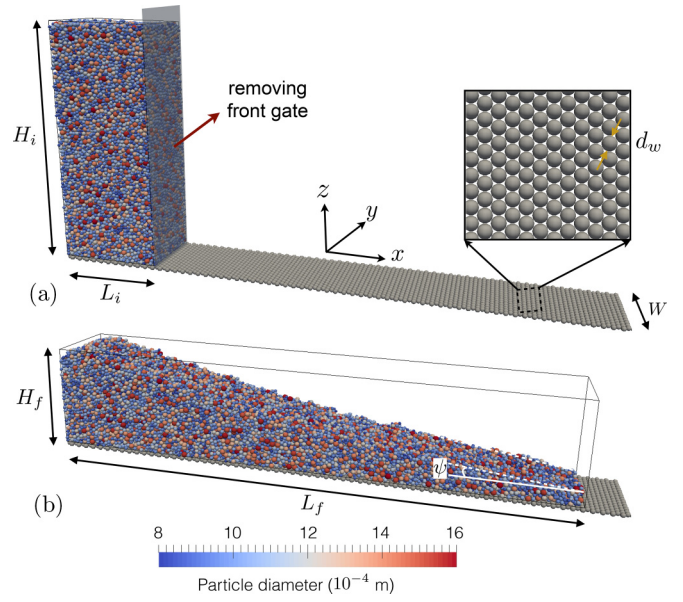


FIG. 1. Numerical model of a viscocohesive granular column with its initial height  $H_i$  and length  $L_i$  (a) collapses on a rough-horizontal plane until reaching a deposition morphology with the final height  $H_f$ , length  $L_f$ , and toe angle  $\psi$  (b).

roughness. The liquid viscous force is then given by

$$f_v = \frac{3}{2}\pi R^2 \eta \frac{v_n}{\delta_n + \delta_{n0}} \quad \text{for } \delta_n > 0. \quad (9)$$

The viscous force tends to reach the largest value when occurs the overlap between particles:

$$f_v = \frac{3}{2}\pi R^2 \eta \frac{v_n}{\delta_{n0}} \quad \text{for } \delta_n \leq 0. \quad (10)$$

In all simulations,  $\delta_{n0}$  is set to  $5 \times 10^{-4} d_{\text{min}}$ , where  $d_{\text{min}}$  is the smallest diameter of primary particle.

## B. Model setting and parameters

To create dense packings of low-viscocoheresive granular columns collapsing on a rough-horizontal plane with different initial column aspect ratio  $a = H_i/L_i$ , as shown in Fig. 1(a), where  $H_i$  and  $L_i$  are the initial height and length of granular column, we first prepared a loose configuration of 31 500 dry particles inside a rectangle in the case of without considering the particles' gravity. The particle diameter is varied in a range  $[d_{\text{min}}, d_{\text{max}} = 2 \times d_{\text{min}}]$ , randomly distributed using the particle volume fraction to avoid the crystallization effects of material, where  $d_{\text{max}}$  and  $d_{\text{min}}$  are the largest and smallest particle diameter. The rectangle is then subjected to the quasistatic compression by imposing different compressive velocities (proportional to its initial thickness) to all side walls until reaching a quite dense packing of particles (the solid fraction is about 0.45). Two lateral walls along the  $y$  direction are then removed and replaced by the periodic boundary conditions as well as setting all particles down to a rough-horizontal plane under their gravity and removing the walls along the  $z$  direction until reaching a dense packing with its solid fraction  $\phi \approx 0.59$ . The rough-horizontal plane is defined by gluing an array of monodisperse particles.

TABLE I. Principal parameters used in the simulations

Parameter	Symbol	Value	Unit
Initial column aspect ratio	$a$	{1.0, 2.0, 2.4}	
Smallest particle diameter	$d_{\min}$	800	$\mu\text{m}$
Largest particle diameter	$d_{\max}$	1600	$\mu\text{m}$
Particle density	$\rho_s$	2600	$\text{kg m}^{-3}$
Coefficient of friction	$\mu$	0.3	
Normal stiffness	$k_n$	$10^6$	N/m
Tangential stiffness	$k_t$	$8 \times 10^5$	N/m
Normal damping	$\gamma_n$	0.8	Ns/m
Tangential damping	$\gamma_t$	0.8	Ns/m
Liquid viscosity	$\eta$	[0,1200]	mPa s
Cohesive stress	$\sigma_c$	[0,117.5]	Pa
Contact angle	$\theta$	0	$^\circ$
Time step	$\Delta t$	$1.5 \times 10^{-7}$	s

Different granular columns with their initial aspect ratio are then extracted from the initial dense packing. In these steps, the friction coefficient between particles and walls is absent. The capillary cohesive forces and viscous forces are activated homogeneously between grains with the gap not to exceed the rupture distance  $d_{\text{rupt}}$  to reach an equilibrium before generating the collapse test.

To generate the collapse of the above granular column on a rough-horizontal surface, the front wall (gate) is immediately removed. The particles start to collapse down under their gravity, then heap and spread along  $x$  direction until reaching a deposit with its final-stage runout distance ( $L_f$ ),

final-stage deposition height ( $H_f$ ), and toe angle  $\psi$ , as shown in Fig. 1(b). These phenomena are well consistent with previous observations in numerical and experimental works for both dry and wet granular materials [37,39,41]. The collapse dynamics and deposition morphology of such a granular column may strongly depend on the initial column aspect ratio  $a$  and cohesive and viscous properties of the fluid. In our simulations we considered low-viscocohesive granular columns using three different initial aspect ratios  $a = \{1.0, 2.0, 2.4\}$ , the cohesive stress  $\sigma_c \approx \kappa/\langle d \rangle$  is varied in a broad range [0.0,117.5] Pa, and the liquid viscosity  $\eta$  is used in a range [0,1200] mPa s, where  $\langle d \rangle$  denotes the mean particle diameter. The sliding friction coefficient between particles and particles, rough-horizontal plane, and behind the wall is set to 0.3, 0.2, and 0.1, respectively. The particle size basically leads to enhancement the mobility and runout distance of wet granular column collapse because the increase in the size of particles has the same effect of decreasing the cohesive stress between them [72]. The particles' gravity may modify the collapse dynamics and deposition morphology, while the initial solid fraction of the column may affect differently depending on initial column aspect ratio. However, in the ongoing work, we aim to evaluate the effects of the initial column aspect ratio and liquid properties on the flow mobilities and deposition morphology thus keeping the same particles' gravity and density, and using one case of particle size distribution is indispensable. All other simulated parameters are given in Table I.

Figures 2(a), 2(b), and 2(c) show a sequence of snapshots of the deposition morphology during the collapse of granular

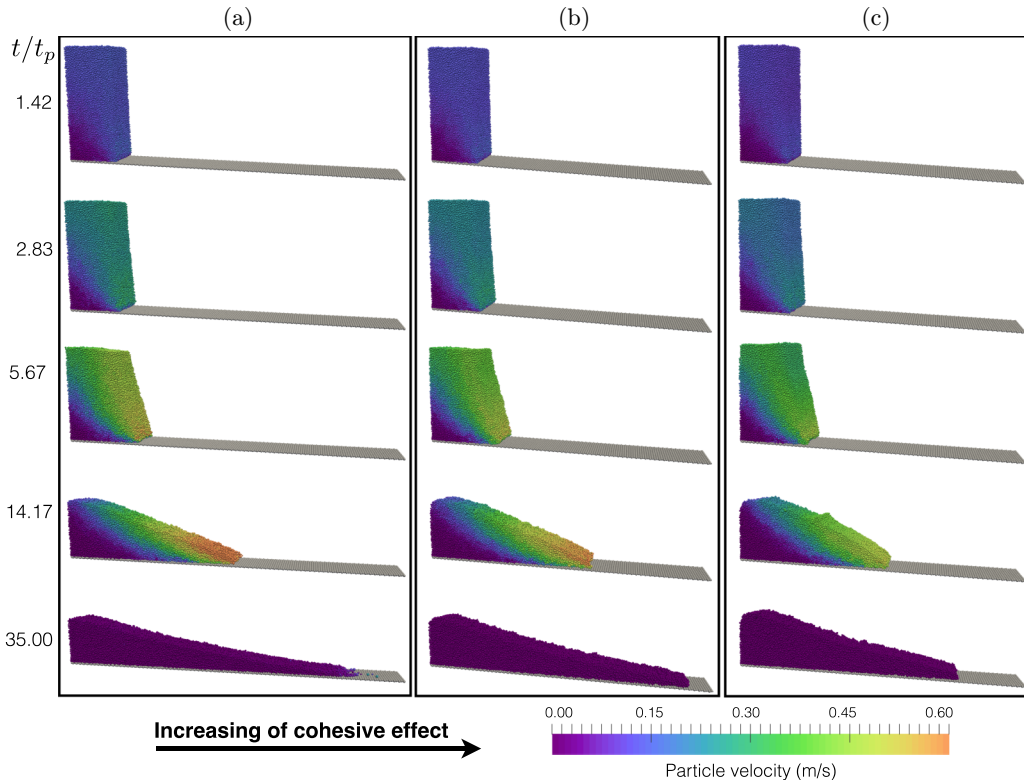


FIG. 2. Sequence of snapshots of a viscocohesive granular column that collapses in different times with different values of the cohesive stress  $\sigma_c$ : 0.059 Pa (a), 26.443 Pa (b), and 88.142 Pa (c) for a given value of the liquid viscosity  $\eta = 100$  mPa s and  $a = 2.4$ .

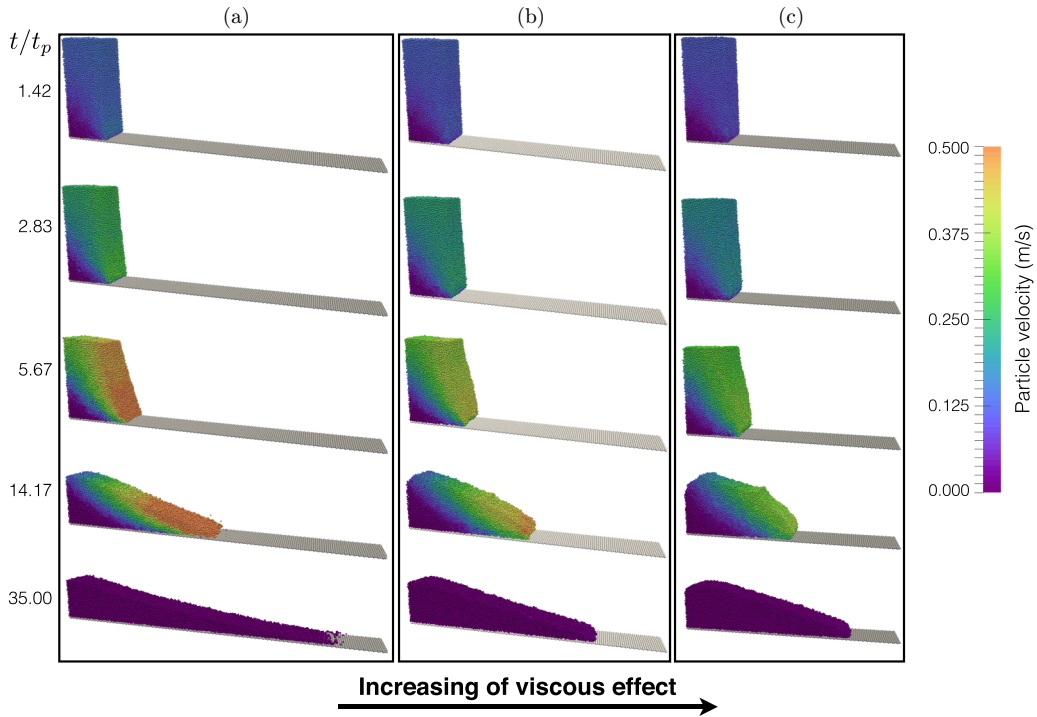


FIG. 3. Snapshots of flow evolution of a viscohesive granular column collapse in a rough-horizontal plane for different values of the liquid viscosity  $\eta = 50$  mPa s (a), 500 mPa s (b), and 1200 mPa s (c) with a given value of the cohesive stress  $\sigma_c = 1.028$  Pa.

column for three different values of the cohesive stress  $\sigma_c$  with a given value of the liquid viscosity  $\eta = 100$  mPa s and initial column aspect ratio  $a = 2.4$ . It is evident that the cohesive stress  $\sigma_c$  strongly affects the collapse and runout dynamics of granular materials at different normalized failure time instants  $t/t_p$  during the process, where  $t$  and  $t_p = (\langle d \rangle / g)^{1/2}$  are the failure time instant and the time of particle with mean diameter  $\langle d \rangle$  which free falls down over a distance  $\langle d \rangle$  under its gravity. In particular, at  $t/t_p = 1.42$ , the collapse of the viscohesive granular column is triggered, and a part of the column starts to flow under the particles' gravity; the column of granular materials is then obviously divided into two different regions at the time around  $t/t_p = 2.83$ : the immobile zone is located at the corner, which is delimited by the behind wall, horizontal plane, and the flowing zone. At these beginning stages, the particles' velocity in the flowing zone of the case of weak interparticle cohesion is slightly higher than that of the strong cohesion cases. For further stages ( $t/t_p = 5.67$ , for instance), the collapse of such viscohesive granular columns is well developed, and the particles' velocity for the case of low cohesion is strongly higher than that for the case of strong cohesion. As a consequence, the spreading speed and runout distance of granular materials decrease significantly with increasing the cohesive stress between grains; these may be explained due to the tensile effects and absorption of the kinetic energy within capillary contacts during the flows.

Similar to the cohesive effect of the capillary contacts, the viscous effect also strongly modifies the collapse and runout dynamics of the viscohesive column due to the domination of the contractive effects as compared to the extensive effects in dense granular packing. Figures 3(a), 3(b), and 3(c) display the collapse of the viscohesive granular column at different time instants for three different values of the liquid viscosity

$\eta$  with a given cohesive stress  $\sigma_c$  during the collapse process. The collapse speed of such a column decreases with increasing the liquid viscosity, leading to the decrease of the runout distance. More interestingly, meanwhile, the particles mainly flow in whole spreading stages for the cases of low liquid viscosity, and the granular materials are extruded forward only for the cases of high viscosity, leading to the formation of the round toes at the final-stage deposition of material, as shown in Fig. 3(c) at  $t/t_p = 35.00$ .

### III. COLLAPSE DYNAMICS

#### A. Evolution of kinetic energy

To highlight the effects of the cohesive stress  $\sigma_c$  and the liquid viscosity  $\eta$  on the collapse dynamics of low-viscohesive granular columns, the evolution of kinetic energy and the deposition morphology during the collapse are analyzed. Figures 4(a) and 4(b) show the evolution of the mean vertical kinetic energy  $\langle E_z \rangle = \langle mv_z^2/2 \rangle$  and the mean horizontal kinetic energy  $\langle E_x \rangle = \langle mv_x^2/2 \rangle$  per grain, respectively, normalized by the mean value of initial potential energy  $\langle E_{ip} \rangle = \langle m \rangle g \langle h \rangle$  per grain as a function of the normalized collapse time  $t/t_p$  for different values of the cohesive stress  $\sigma_c$ , where  $v_z$  and  $v_x$  are the vertical and horizontal velocities of particles, respectively,  $\langle h \rangle$  denotes the mean initial height of the particles as compared to the horizontal surface. The granular column collapse on a horizontal plane undergoes three different phases: collapse, heap, and spread, which are clearly determined by the evolution and transformation of vertical and horizontal kinetic energies of granular materials [46]. The collapse phase is determined from the beginning of the collapse process until reaching the maximum vertical kinetic

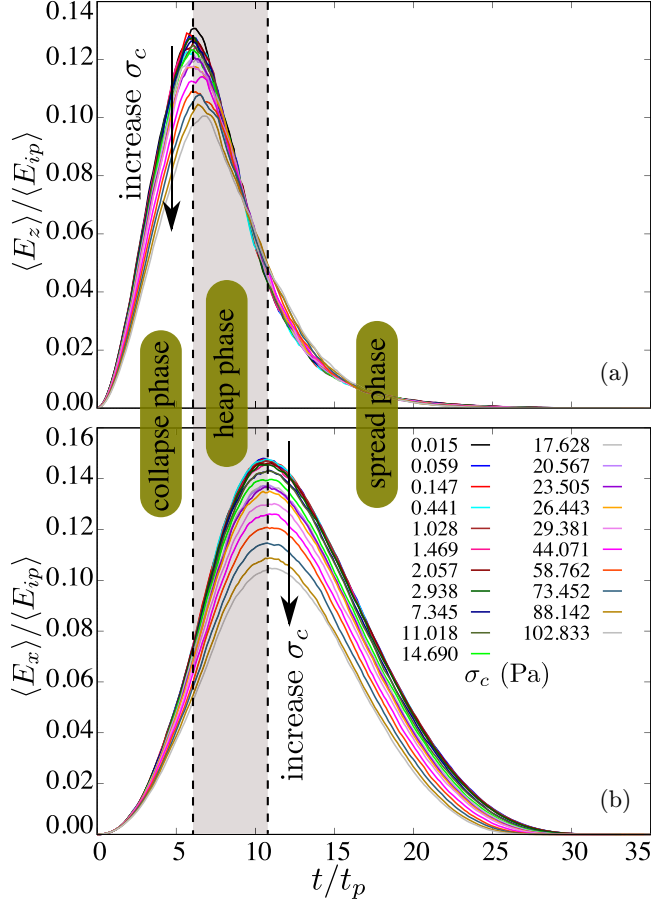


FIG. 4. Evolution of normalized vertical (a) and horizontal (b) kinetic energy per grain by the mean initial potential energy  $E_{ip}$  for different values of the cohesive stress  $\sigma_c$  with a given value of liquid viscosity  $\eta = 100$  mPa.s.

energy, the heap phase is reflected by the transformation of maximum kinetic energies from the vertical direction to the horizontal one, and the spread phase is presented by the reduction of the horizontal kinetic energy from maximum to zero.

In the collapse phase,  $\langle E_z \rangle$  first increases rapidly and reaches a peak that decreases with increasing  $\sigma_c$  under the gravity effect, whereas  $\langle E_x \rangle$  is still small. Passing the collapse regime, marked by the peak of  $\langle E_z \rangle$ , the horizontal kinetic energy then also increases rapidly and reaches the peak value that decreases with increasing  $\sigma_c$ ; meanwhile,  $\langle E_z \rangle$  declines in this regime as a consequence of transforming of  $\langle E_z \rangle$  to  $\langle E_x \rangle$  in the heap stage [46]. After that,  $\langle E_x \rangle$  reduces with the curves, which are almost parallel in a range with  $t/t_p \sim [15, 22]$  in the spreading phase before reaching a final deposit. As compared to the final zero kinetic energy, this reduction rate seems decreasing with increasing  $\sigma_c$ .

Figures 5(a) and 5(b) display the evolution of the normalization  $\langle E_z \rangle / \langle E_{ip} \rangle$  and  $\langle E_x \rangle / \langle E_{ip} \rangle$  as a function of the collapse time  $t/t_p$  for six different values of the liquid viscosity  $\eta$  and for the dry case of granular materials. Similar to the effects of the cohesive stress  $\sigma_c$  on the collapse dynamics of a viscohesive granular column, the liquid viscosity  $\eta$  strongly affects the kinetic energy along both vertical and horizontal directions. Generally, in this current dense packing of such

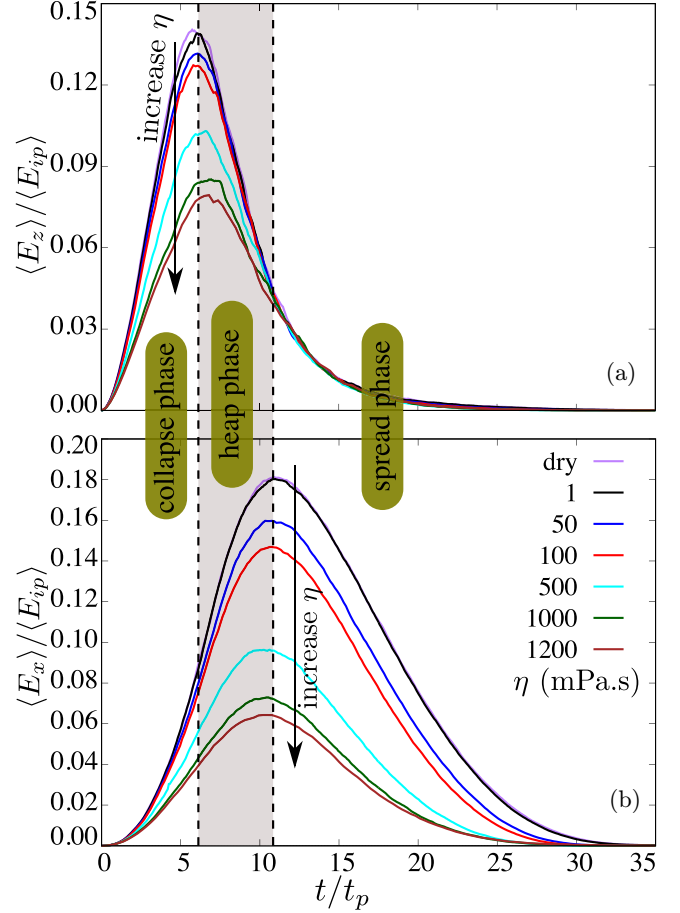


FIG. 5. Normalized vertical (a) and horizontal (b) kinetic energy per grain by the mean initial potential energy  $E_{ip}$  for different values of the liquid viscosity  $\eta$  with a given value of the cohesive stress  $\sigma_c = 1.028$  Pa and for the dry case of granular materials.

a viscohesive granular column, the cohesive stress  $\sigma_c$  and the liquid viscosity  $\eta$  have similar effects on the collapse and runout dynamics due to the domination of the attractive effects of the viscous interactions as compared to their extensive effects. These observations are consistent with previous work that considered the collapse of a granular column in a viscous fluid [46]. Furthermore, due to considering the initial dense packing of a granular column, the kinetic energy of the dry case is higher than that of the viscohesive cases, leading to the longer runout distance and lower deposition height at the final stage, as will be shown below.

## B. Deposition morphology

The paper further analyzes the differences of the morphology profiles of the granular model during the collapse due to the effects of the cohesive stress  $\sigma_c$  and the liquid viscosity  $\eta$ , plotted as the relationship between the normalized deposition height  $Z/H_i$  and normalized spreading distance  $X/L_i$ , as shown in Figs. 6 and 7, where  $Z$  and  $X$  are the instantaneous height and length of granular sample during the collapse process, respectively. In Fig. 6, with the initial column aspect ratio  $a = 2.4$ , the morphology profiles of granular materials differ during the collapse depending on the magnitude of

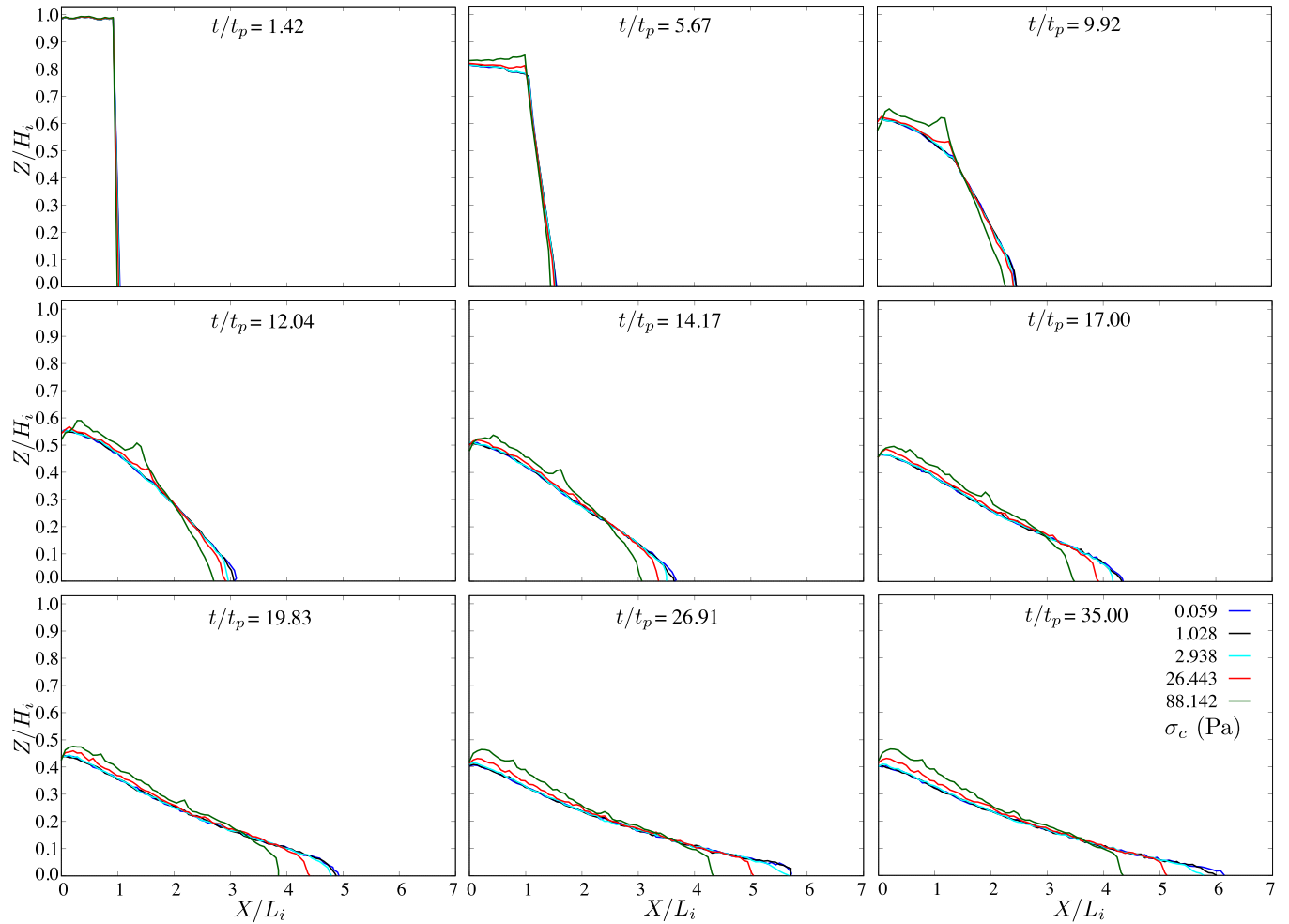


FIG. 6. Evolution of the deposition morphology of a visco-cohesive granular column collapse on a rough-horizontal plane for five different values of  $\sigma_c$  with a given value of liquid viscosity  $\eta = 100$  mPa s.

the cohesive stress  $\sigma_c$ . When  $\sigma_c$  is small (corresponding to  $\sigma_c = 0.059, 1.028$ , or  $2.938$  Pa, for instance) for the case of  $\eta = 100$  mPa s, the particles on the top of the column initially collapse and flow downward as well as push the lower grains forward. This leads to the formation of the inclined top-free surface of the column in the latter steps, as shown in top-middle plot in Fig. 6 (at  $t/t_p = 5.67$ ) and in Fig. 2. We then can see the same transition of these morphology profiles, finally reaching a final deposition morphology with a smooth surface in the whole width range of movements and sharp toes [45], as shown in right-bottom plot of Fig. 6.

The above observations are slightly different as compared to the case of considering a high value of cohesive stress  $\sigma_c$ . Indeed,  $\sigma_c = 88.142$  Pa, for instance, all top particles initially push the lower particles downward but slightly collapsing as a consequence of strong adhesion between grains, leading to the extrusive movements of particles that are closely located near the bottom. For the next stages, instead of separately collapsing and flowing the particles on the top of the column, a layer of top particles is divided into two different parts: the right part rotates counterclockwise and the left one is clockwise, while the lower particles are continuously extruding forward as a consequence of considering the strong cohesion between grains, as shown in Fig. 6 with  $t/t_p$  up to 14.17. This can be

called a block collapse, as reported in [36,41]. These phenomena are also similarly obtained for the high values of the liquid viscosity ( $\eta = 1200$  mPa s, for instance) due to the strong contribution of the contractive effects of the viscous fluid, as shown in Fig. 7 for the red line with  $t/t_p$  up to 19.83. The extrusive behavior of highly visco-cohesive granular column collapse leads to obtaining a round toe at the final deposition stage of granular materials instead of a quite ambiguous shape for dry or low-cohesive granular materials.

The appearance of different collapse behavior of low-visco-cohesive granular columns on a rough-horizontal surface is consistent due to the effects of the initial column aspect ratio, cohesive stress, and liquid viscosity of the binding liquid. Figures 8(a) and 8(b) display the dependence of the final deposition height and the final runout distance, respectively, as a function of  $\sigma_c$  for different values of  $a$  and  $\eta$ . Considering a whole range values of  $\sigma_c$ , the tendency of the evolution of  $H_f/H_i$  and  $(L_f - L_i)/L_i$  is similar for different cases of the liquid viscosity and aspect ratio  $a$ , which represent a slight influence for low cohesive stress ( $\sigma_c < 10$  Pa) and a significant dependence for higher ones. As discussed above, the aspect ratio  $a$  and liquid viscosity  $\eta$  are also strongly modified the deposition morphology of low-visco-cohesive granular column collapse, characterized by the significant increase of  $H_f/H_i$

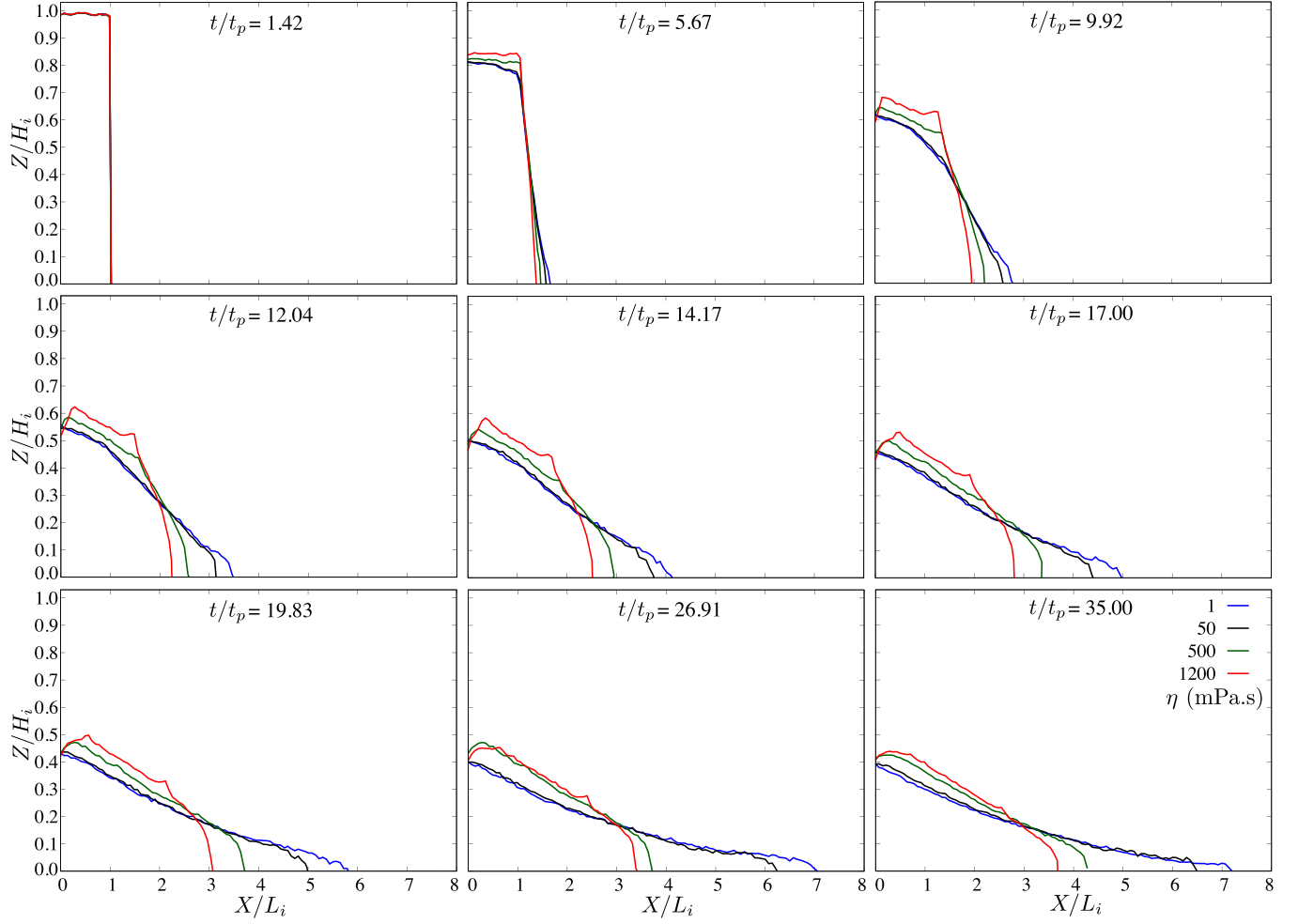


FIG. 7. Deposition morphology of the column collapse for five different values of the liquid viscosity  $\eta$  with a given value of the cohesive stress  $\sigma_c = 1.028\text{Pa}$ .

and decrease of  $L_f/L_i$  with increasing  $\eta$ , and the decrease of  $H_f/H_i$  and enhancement of  $L_f/L_i$  with increasing  $a$  for each value of  $\sigma_c$ . These may be explained due to the strong domination of the extensive effects of the viscous liquid for the low cohesive case, leading to the stronger mobility of granular materials; meanwhile the deposition morphology tends to be complicated for strong cohesive effect. All these complex observations may be due to the compensation between cohesive effect and contraction effect of the liquid binding as well as the compensation between inertial effect of the flows and extension effect of the fluid phase.

#### IV. SCALING BEHAVIOR OF KINETIC ENERGY AND DEPOSITION MORPHOLOGY

Although the initial aspect ratio  $a$  and the liquid properties (cohesive stress  $\sigma_c$  and liquid viscosity  $\eta$ ) affect differently the kinetic energy and deposition morphology, there are similar tendencies of the evolution of maximum values of mean vertical kinetic energy  $\langle E_z \rangle_{\max}/\langle E_{ip} \rangle$ , maximum values of mean horizontal kinetic energy  $\langle E_x \rangle_{\max}/\langle E_{ip} \rangle$ , normalized deposition height  $H_f/H_i$ , and normalized runout distance  $(L_f - L_i)/L_i$  for each value of  $a$ ,  $\sigma_c$ , and  $\eta$ . These observations lead to the question of whether it is possible to describe the

physical quantities above by a dimensionless parameter that incorporates the column morphology and liquid properties. To address this interesting conjecture, the definition of a new scaling parameter is first considered in this section.

As reported in Artoni *et al.* [72] in considering the collapse of wet granular columns, the deposition morphology can be described by using the Bond number  $\text{Bo}$ , defined as a ratio between the gravitational force and the cohesive force exerted on mean particle diameter. However, the effects of the initial column aspect ratio on the deposition morphology of wet granular column collapses were neglected in their descriptions. In unchanneled collapse of wet granular columns in the pendular regime, Li *et al.* [61] further considered the effects of initial column aspect ratio on the scaling behavior of the deposit height, runout distance, and deposit area. Although the observations reported by Li *et al.* [61] basically described the deposit height and runout distance as a function of the initial aspect ratio by modifying these physical quantities using the Bond number, these scalings have not yet provided a unified description between the deposition morphology and affected parameters. More recently, Wu *et al.* [62] defined a dimensionless cohesion number, incorporating the Bond number and system size (the size between the initial column height and particle diameter), allowing one



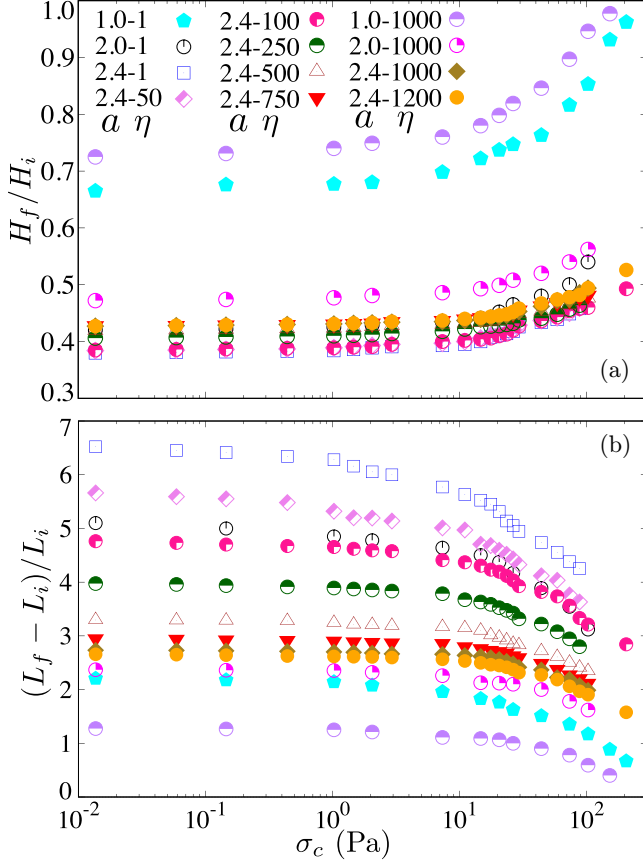


FIG. 8. (a) Normalized final deposition height  $H_f/H_i$  and (b) normalized final runout distance  $(L_f - L_i)/L_i$  as a function of the cohesive stress  $\sigma_c$  between particles for different values of the initial column aspect ratio  $a$  and the liquid viscosity  $\eta$  (mPa s).

to describe the deposit height, runout distance, and surface roughness of the deposit. But does this dimensionless cohesion number also control the collapse dynamics and spreading behavior of wet granular columns? Following the above observations, to provide unified descriptions of the collapse mobilities, spreading behavior, and deposition morphology of gravity-driven viscohesive granular column collapse on a horizontal plane, we reintroduce the dimensionless scaling parameter. This number is defined as a ratio of the cohesive stress  $\sigma_c$  and the mean confining stress  $\langle\sigma_p\rangle$  exerted on grain having mean diameter  $\langle d\rangle$ . Due to keeping the same value of  $L_i$  and without changing the particle size,  $\langle\sigma_p\rangle$  can be related to  $a$ , implying the scaling dimensionless number is the combination between the Bond number  $\text{Bo}$  and initial column aspect ratio  $a$ , as given in the following:

$$\Upsilon \equiv \frac{\sigma_c}{\langle\sigma_p\rangle} \equiv \frac{\sigma_c}{a \times \langle\sigma_n\rangle} \simeq \text{Bo}^{-1} a^{-1}, \quad (11)$$

where  $\sigma_c \sim \kappa/\langle d\rangle$ ,  $\langle\sigma_n\rangle \sim \langle m\rangle g/\langle d\rangle^2$ , and  $\text{Bo} = \rho_s g \langle d\rangle^2/\kappa$ ,  $\langle m\rangle$  denotes the mean mass of grains. The definition of this dimensionless number ( $\Upsilon$ ) based on the above stresses is more easily controlled than the effective cohesion parameter defined by Mandal and co-workers [26] because it depends on the dissipation and stiffness of grains and the cohesion between particles.

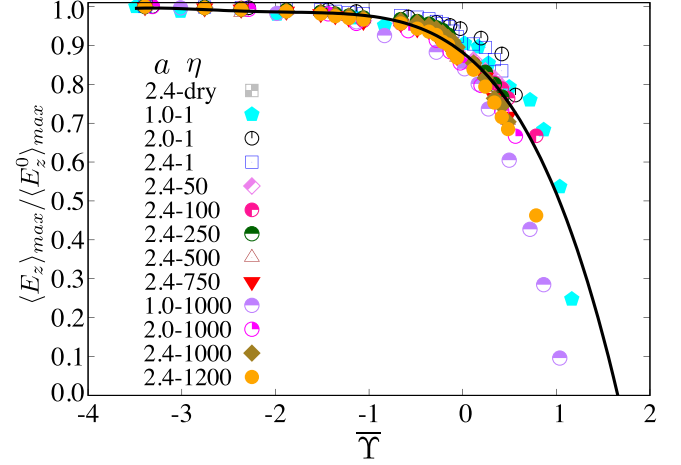


FIG. 9. Maximum value of mean vertical kinetic energy per grain  $\langle E_z \rangle_{\max}$  normalized by that of the noncohesive case  $\langle E_z^0 \rangle_{\max}$  as a function of the dimensionless parameter  $\Upsilon = \log_{10}(\Upsilon)$  for all our simulations. The solid line is the analytical expression of Eq. (13). Each symbol and its colors in the legend are shown with initial column aspect ratio  $a$  and the liquid viscosity  $\eta$ , respectively.

Figures 9 and 10 reveal the correlations between the normalized maximum values of mean vertical kinetic energy  $\langle E_z \rangle_{\max}/\langle E_z^0 \rangle_{\max}$  and normalized maximum values of mean horizontal kinetic energy  $\langle E_x \rangle_{\max}/\langle E_x^0 \rangle_{\max}$ , respectively, with the new dimensionless number  $\Upsilon = \log_{10}(\Upsilon)$  for all our simulations of varying different values of the initial aspect ratio  $a$ , cohesive stress  $\sigma_c$ , and liquid viscosity  $\eta$ , where  $\langle E_z^0 \rangle_{\max}$  and  $\langle E_x^0 \rangle_{\max}$  denote the maximum value of the mean vertical and horizontal kinetic energy in the case of without cohesion, respectively. It is interesting to see that all the data points of  $\langle E_z \rangle_{\max}/\langle E_z^0 \rangle_{\max}$  and  $\langle E_x \rangle_{\max}/\langle E_x^0 \rangle_{\max}$  are nicely controlled by  $\Upsilon$ . These descriptions show an agreement with previous experimental observations reported by Artoni *et al.* [72] and

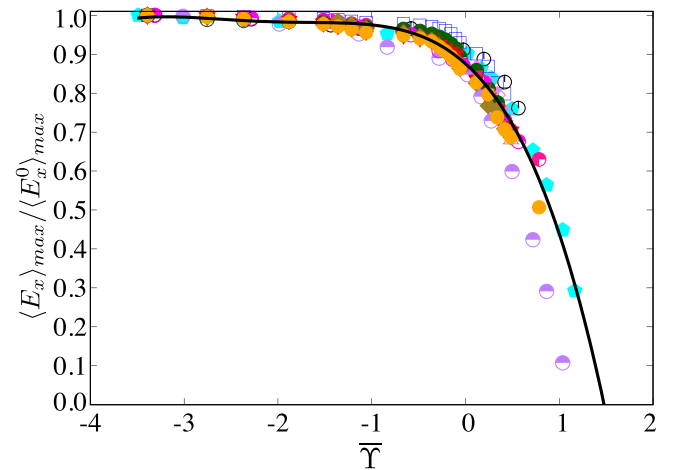


FIG. 10. Maximum value of mean horizontal kinetic energy per grain  $\langle E_x \rangle_{\max}$  normalized by that of the noncohesive case  $\langle E_x^0 \rangle_{\max}$  as a function of the dimensionless parameter  $\Upsilon = \log_{10}(\Upsilon)$  for all our simulations. The symbols and their colors are the same as those in Fig. 9.

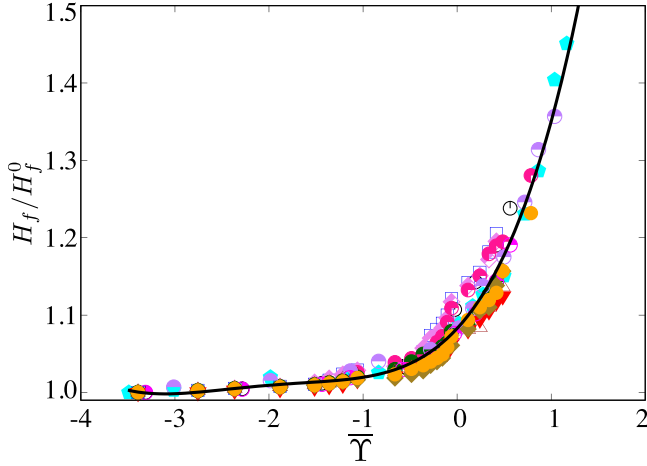


FIG. 11. Normalized deposition height  $H_f/H_f^0$  as a function of the dimensionless parameter  $\bar{\Upsilon} = \log_{10}(\Upsilon)$  for all our simulations. The solid line is the analytical expression of Eq. (13). The symbols and their colors are the same as those in Fig. 9.

Li *et al.* [61]. Interestingly, all values of  $\langle E_z \rangle_{\max}/\langle E_z^0 \rangle_{\max}$  and  $\langle E_x \rangle_{\max}/\langle E_x^0 \rangle_{\max}$  obtained in our simulations are fitted by the same function form but with different setting values of prefactors, which correspond to the effects of three different key parameters during the collapse process. The general fitting function form is given by Eq. (13):

$$\frac{A}{B} = a_4 \bar{\Upsilon}^4 + a_3 \bar{\Upsilon}^3 + a_2 \bar{\Upsilon}^2 + a_1 \bar{\Upsilon} + a_0, \quad (12)$$

where  $A/B \equiv \langle E_z \rangle_{\max}/\langle E_z^0 \rangle_{\max}$ ,  $a_0 = 0.8817$ ,  $a_1 = -0.1888$ ,  $a_2 = -0.1299$ ,  $a_3 = -0.0394$ , and  $a_4 = -0.0043$  for describing the normalized vertical kinetic energy  $\langle E_z \rangle_{\max}/\langle E_z^0 \rangle_{\max}$  in the collapse stage, and  $A/B \equiv \langle E_x \rangle_{\max}/\langle E_x^0 \rangle_{\max}$ ,  $a_0 = 0.8757$ ,  $a_1 = -0.2150$ ,  $a_2 = -0.1625$ ,  $a_3 = -0.0533$ , and  $a_4 = -0.0062$  for describing the normalized horizontal kinetic energy  $\langle E_x \rangle_{\max}/\langle E_x^0 \rangle_{\max}$  in the heap stage. These excellent fittings are strongly supported by high coefficients of determination  $R^2$ , 90.88% and 95.31%, respectively.

As discussed in Sec. III, the collapse process of a granular column undergoes three different phases: (1) collapse, (2) heap, and (3) spread and deposition. The spread and deposition stage can be featured by the final deposition morphology of granular flows, characterized by its final deposition height and final runout distance. Although normalized kinetic energy obtained in the collapse and heap phase can be well described as a function of  $\bar{\Upsilon}$  with interesting contributions of the initial column aspect ratio and the cohesive effects of the binding liquid, the deposition morphology of granular column collapse also should be quantitative in the deposit stage. Interestingly, the normalized final deposition height  $H_f/H_f^0$  and normalized final runout distance  $(L_f - L_i)/(L_f^0 - L_i)$  are nicely scaled by the same dimensionless parameter  $\bar{\Upsilon}$ , as respectively displayed in Figs. 11 and 12, where  $H_f^0$  and  $L_f^0$  are the final deposition height and runout distance of noncohesive granular columns. These findings robustly confirm for the unified descriptions of the physical quantities by incorporating the Bond number and initial column aspect ratio not only in the

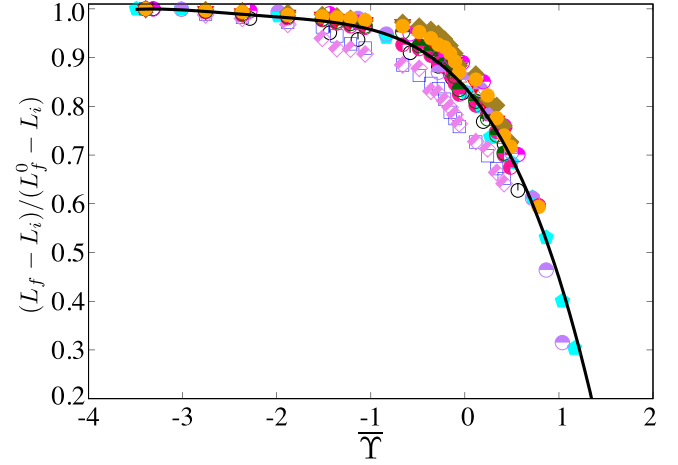


FIG. 12. Normalized runout distance  $(L_f - L_i)/(L_f^0 - L_i)$  as a function of the dimensionless parameter  $\bar{\Upsilon} = \log_{10}(\Upsilon)$  for all our simulations. The solid line is the analytical expression of Eq. (13). The symbols and their colors are the same as those in Fig. 9.

collapse and heap stage but also in the deposition stage of gravity-driven low-viscocohesive granular column collapse on a horizontal plane.

It is interesting to see that all the data points of  $H_f/H_f^0$  (Fig. 11) and  $(L_f - L_i)/(L_f^0 - L_i)$  (Fig. 12) are also fitted using the same function form expressed by Eq. (13) but with different values of prefactors. In particular, referring to Eq. (13),  $A/B \equiv H_f/H_f^0$ ,  $a_0 = 1.0827$ ,  $a_1 = 0.1319$ ,  $a_2 = 0.0982$ ,  $a_3 = 0.0335$ , and  $a_4 = 0.0041$  for describing the normalized final deposition height  $H_f/H_f^0$ ; and  $A/B \equiv (L_f - L_i)/(L_f^0 - L_i)$ ,  $a_0 = 0.8388$ ,  $a_1 = -0.2168$ ,  $a_2 = -0.1320$ ,  $a_3 = -0.0381$ , and  $a_4 = -0.0041$  for introducing the normalized final runout distance  $(L_f - L_i)/(L_f^0 - L_i)$ . These fittings of  $H_f/H_f^0$  and  $(L_f - L_i)/(L_f^0 - L_i)$  are strongly reinforced by high coefficients of determination  $R^2$ , 93.31% and 91.16% respectively.

Besides classically considering the deposition height and runout distance, the effects of input parameters on the collapse dynamics and deposition morphology can also be highlighted by measuring the the half runout time  $t_{0.5}$  and the toe angle  $\psi$  in the final deposition stage (shown in Fig. 1), where  $t_{0.5}$  is the time of granular flows reaching half of the runout distance, as previously defined by Artoni *et al.* [72]. As expected, the unified description of the collapse dynamics is strongly evidenced by the quite good expression of the normalized half runout time  $t_{0.5}/t_{0.5}^0$  as a function of the same dimensionless number  $\bar{\Upsilon} = \log_{10}(\Upsilon)$  for all values of the principal parameters, as shown in Fig. 13, where  $t_{0.5}^0$  denotes the time that a noncohesive granular column reaches half of its runout distance. This correlation is similar to the relationship between the normalized kinetic energy and  $\bar{\Upsilon}$  and the runout distance and  $\bar{\Upsilon}$ , as respectively shown in Figs. 10 and 12. Remarkably, the  $t_{0.5}/t_{0.5}^0$  vs  $\bar{\Upsilon}$  correlation is also agreeably fitted using the general fitting function form [Eq. (13)], where  $A/B \equiv t_{0.5}/t_{0.5}^0$ ,  $a_0 = 0.9472$ ,  $a_1 = -0.0501$ ,  $a_2 = -0.0164$ ,  $a_3 = -0.0015$ , and  $a_4 = 0.0001$ . This fitting is reinforced by the coefficient of determination  $R^2 = 88.47\%$ .

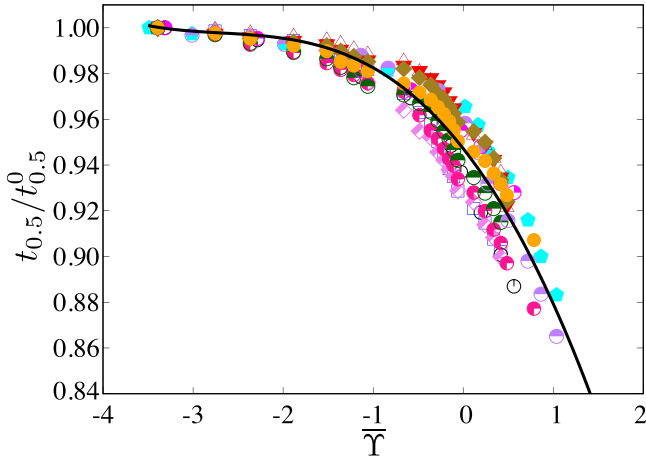


FIG. 13. Normalized half runout time  $t_{0.5}/t_{0.5}^0$  as a function of the scaling dimensionless parameter  $\bar{\Upsilon} = \log_{10}(\Upsilon)$  for all cases of the simulations. The solid line is the analytical expression of Eq. (13).

Although the deposition morphology of granular column collapse is normally characterized by its deposition height and runout distance, the morphology of the free surface also should be quantitative to highlight the effects of liquid properties. As documented by Abramian *et al.* [45], the roughness of the free surface is strongly modified by the cohesive stress between grains. In particular, this roughness of the final deposit increases with increasing the cohesive effects of the material. Artoni *et al.* [72] have measured the toe angle of the final deposit of a wet granular column collapse, and their results introduced a correlation between this angle and the Bond number. However, in the case of the liquid viscosity comes into play with the cohesive effects, and the toe angle  $\psi$  may represent significantly complex properties. Figure 14 displays the evolution of normalized toe angle  $\psi/\psi^0$  as a function of  $\bar{\Upsilon}$  for all our simulations in semilog scale, where  $\psi^0$  is the toe angle of the simulation in the case of not considering the cohesion between grains. This correlation is described using

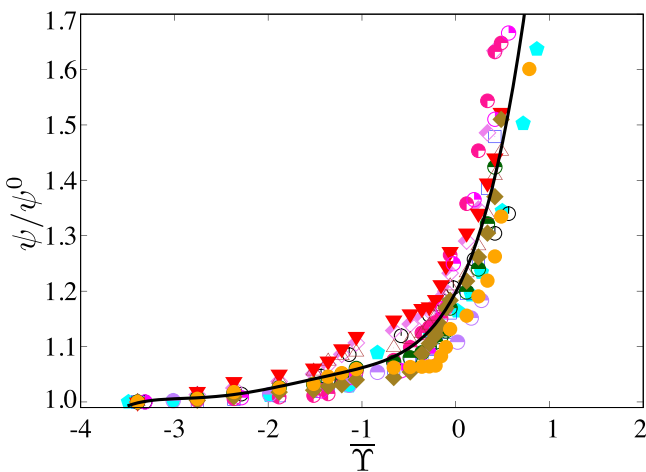


FIG. 14. Normalized deposition angle  $\psi/\psi^0$  as a function of the scaling dimensionless parameter  $\bar{\Upsilon} = \log_{10}(\Upsilon)$  for all our simulations. The solid line is the analytical expression of Eq. (13).

the following fitting function form:

$$\frac{\psi}{\psi^0} = a_5 \bar{\Upsilon}^5 + a_4 \bar{\Upsilon}^4 + a_3 \bar{\Upsilon}^3 + a_2 \bar{\Upsilon}^2 + a_1 \bar{\Upsilon} + a_0, \quad (13)$$

where  $a_0 = 1.1980$ ,  $a_1 = 0.3264$ ,  $a_2 = 0.3281$ ,  $a_3 = 0.1815$ ,  $a_4 = 0.0484$ , and  $a_5 = 0.0049$ . These chosen prefactors of the above-functional fitting [Eq. (13)] and the data points of the toe angle obtained in our simulations are supported by a value of a coefficient of determination  $R^2 = 88.04\%$ . This coefficient is slightly smaller than the coefficients of determination of the scalings observed for the final deposition height and final runout distance because the toe angle may not only strongly depend on the cohesive and viscous effects but also cannot be eventually characterized for the evolution of the free surface of a granular deposit.

## V. DISCUSSION

Physical meanings behind the above-unified descriptions may be clarified based on the opposite effects of the initial column aspect ratio and the cohesive stress between grains as well as the compensation between the cohesive and viscous effects during the collapse process. As we know, when the cohesive, viscous, and inertial effects together come into play, the flows (mobilities) of granular materials are complicated; one may delay the flows due to the contraction behavior of the viscosity and cohesion, another one may enhance mobilities of granular materials as a consequence of the lubrication effect or the extension effect of the liquid. In the model of gravity-driven low-viscocohesive granular column collapse on a rigid-horizontal surface, the collapse dynamics characterized by the energy evolution and half runout time and deposition morphology characterized by the deposition height, runout distance, and toe angle are governed by the initial column aspect ratio and the cohesive stress, represented via the combination between the Bond number and the aspect ratio. Indeed, the low-viscocohesive granular column collapses under the gravity effects generating vertical kinetic energy, which pushes grains to undergo the heap phase with the highest horizontal kinetic energy and spread phase before going to rest at a deposit; these phases commonly show the unified effects of the cohesive stress or the compensation between cohesive and viscous effects, leading to similar descriptions of the collapse dynamics and deposition morphology.

From the findings and physical insights above, the current work shows the potential ability to well predict the mechanism of the postfailure landslide and its runout dynamics. The runout distance of landslide or debris flows remains a challenging problem, as illustrated by their unexplained high mobility due to the complex effects of both cohesive and viscous characteristics of the liquid inclusion with the discrete nature of the material and the morphology of the slope or column. Theoretically, the runout distance of granular flows induced from landslides or debris avalanches is reduced due to the cohesive effects of the liquid; however, this landslide or debris characteristic reveals complex behavior due to the inclusion of the viscous effects of the liquid as a consequence of containing the compensation between the inertial effects

of material and viscous effects of the liquid as well as the compensation between the cohesive effects and viscous effects. Thus, our results suggested an appropriate prediction of the final deposition morphology of gravity-induced landslides by defining a new dimensionless parameter that incorporates the Bond number and the intrinsic parameter as the initial column aspect ratio.

Our simulations have shown interesting observations and consistency with the previous simulations and experiments [61,62,72]. However, to reflect more directly on the phenomena of natural disasters, the numerical simulations may be extendable to different configurations such as the convex and concave sliding surfaces to investigate the full process of landslide failure [73,74] or different material and operational conditions such as particle properties, particle density, particle size, solid packing fraction, and sliding volume in the case of considering more realistic soil properties. The numerical simulations may be also extended to study the saturated regime of grain-fluid mixtures, where the pore water pressure plays a significant role in the enhancement of the mobility of granular materials compensated with grain inertia.

## VI. SUMMARY AND CONCLUSIONS

This paper presents a series of discrete element simulations of low-viscocohesive granular columns collapse on a rough-horizontal surface to comprehensively investigate their collapse dynamics and deposition morphology under the effects of the cohesive and viscous properties of the binding liquid and initial column aspect ratio. Each granular sample is constructed by generating a column of spherical particles and using the periodic boundary conditions. All particle interactions are modeled using the contact force law, which contains the elastic and frictional forces in addition to the cohesive and viscous contacts due to the presence of the liquid binding. In this current work, the liquid is assumed to be initially homogeneously distributed with the reversible consideration of the capillary bridges during the failure process. The collapse dynamics of low-viscocohesive granular columns are characterized by the evolution of kinetic energies in vertical and horizontal directions and the half runout time, while the final

deposition morphology is featured by the deposition height, runout distance, and toe angle.

The results show that the collapse dynamics of such columns undergo different phases (collapse, heap, spread, and deposition) and represent complex behavior during the failure process; these may be due to the complicated influences of the cohesive and viscous properties of the binding liquid. As expected, the low-viscocohesive granular column with a higher initial aspect ratio induces higher kinetic energies (in both vertical and horizontal directions) and longer runout distance but lower deposition height and smaller toe angle, while stronger cohesive forces and viscous forces generate higher deposition height and larger toe angle but lower kinetic energy and shorter runout distance. Interestingly, all data points of normalized vertical and horizontal kinetic energy, normalized half runout time, normalized deposition height, normalized runout distance, and normalized toe angle are excellently described under a nontrivially unified description as a polynomial function of the new dimensionless number, which incorporates the Bond number and the initial column aspect ratio. However, the physical property (toe angle) characterized for the free surface of the final deposit is nicely scaled with a different fitting function as compared to other physical quantities. This difference may be explained by the strong influence of the cohesive stress as well as the difficulty of using the toe angle for eventually characterizing the free surface morphology in the deposition stage. Although the findings provide the unified descriptions of the flow mobilities and deposition morphology of viscocohesive granular column collapse, the results were obtained only for low-viscocohesive granular columns with low cohesion in the pendular regime; this is evident by the nonmonotonic polynomial fitting functions used for describing physical quantities.

## ACKNOWLEDGMENTS

This research is funded by Vietnam National Foundation for Science and Technology Development (NAFOSTED) under Grant No. 107.01-2021.23.

The authors confirm that there is no conflict of interest to declare.

- 
- [1] D. P. Kanungo, M. K. Arora, R. P. Gupta, and S. Sarkar, *Landslides* **5**, 407 (2008).
  - [2] A. Taboada and N. Estrada, *J. Geophys. Res.: Earth Surface* **114**, F03004 (2009).
  - [3] D. B. Kirschbaum, R. Adler, Y. Hong, S. Hill, and A. Lerner-Lam, *Nat. Hazards* **52**, 561 (2010).
  - [4] G. Martelloni, F. Bagnoli, and E. Massaro, *Commun. Nonlinear Sci. Numer. Simul.* **18**, 2479 (2013).
  - [5] W. Liao and J. Ji, *Comput. Geotech.* **129**, 103903 (2021).
  - [6] R. Chehade, B. Chevalier, F. Dedecker, P. Breul, and J.-C. Thouret, *Bull. Eng. Geol. Environ.* **80**, 6629 (2021).
  - [7] D. Schneider, C. Huggel, W. Haeberli, and R. Kaitna, *Earth Surf. Proc. Landforms* **36**, 1948 (2011).
  - [8] R. M. Iverson, *Geomorphology* **244**, 9 (2015).
  - [9] Q. Yang, Z. Su, Q. Cheng, Y. Ren, and F. Cai, *Eng. Geol.* **260**, 105260 (2019).
  - [10] H. H. Bui and G. D. Nguyen, *Comput. Geotech.* **138**, 104315 (2021).
  - [11] T.-T. Vo, D. M. Tran, C. T. Nguyen, and T.-K. Nguyen, *Solid State Commun.* **369**, 115190 (2023).
  - [12] T. Mikami, H. Kamiya, and M. Horio, *Chem. Eng. Sci.* **53**, 1927 (1998).
  - [13] S. Iveson, J. Beathe, and N. Page, *Powder Technol.* **127**, 149 (2002).
  - [14] P. Rognon, J.-N. Roux, M. Naaim, and F. Chevoir, *J. Fluid Mech.* **596**, 21 (2008).
  - [15] S. G. Evans, *Canadian Geotech. J.* **26**, 447 (1989).

- [16] H. M. Fritz, F. Mohammed, and J. Yoo, *Pure Appl. Geophys.* **166**, 153 (2009).
- [17] F. Vagnon, M. Pirulli, A. Yague, and M. Pastor, *Can. Geotech. J.* **56**, 89 (2019).
- [18] J. Torres-Serra, E. Romero, and A. Rodríguez-Ferran, *Powder Technol.* **362**, 559 (2020).
- [19] Z. Liu, L. Su, C. Zhang, J. Iqbal, B. Hu, and Z. Dong, *Comput. Geotech.* **123**, 103561 (2020).
- [20] GDR MiDi, *Eur. Phys. J. E* **14**, 341 (2004).
- [21] P. Jop, Y. Forterre, and O. Pouliquen, *Nature (London)* **441**, 727 (2006).
- [22] O. Pouliquen, C. Cassar, P. Jop, Y. Forterre, and M. Nicolas, *J. Stat. Mech.* (2006) P07020.
- [23] Y. Forterre and O. Pouliquen, *Annu. Rev. Fluid Mech.* **40**, 1 (2008).
- [24] P. Fu and Y. F. Dafalias, *Intl. J. Numer. Anal. Methods Geomech.* **35**, 1098 (2011).
- [25] M. Trulsson, B. Andreotti, and P. Claudin, *Phys. Rev. Lett.* **109**, 118305 (2012).
- [26] S. Mandal, M. Nicolas, and O. Pouliquen, *Proc. Natl. Acad. Sci. USA* **117**, 8366 (2020).
- [27] T.-T. Vo, S. Nezamabadi, P. Mutabaruka, J.-Y. Delenne, and F. Radjai, *Nat. Commun.* **11**, 1476 (2020).
- [28] G. Lube, H. E. Huppert, R. S. J. Sparks, and A. Freundt, *Phys. Rev. E* **72**, 041301 (2005).
- [29] E. Lajeunesse, J. B. Monnier, and G. M. Homsy, *Phys. Fluids* **17**, 103302 (2005).
- [30] E. L. Thompson and H. E. Huppert, *J. Fluid Mech.* **575**, 177 (2007).
- [31] C. T. Nguyen, C. T. Nguyen, H. H. Bui, G. D. Nguyen, and R. Fukagawa, *Landslides* **14**, 69 (2017).
- [32] Q. Zhang, B.-I. Huang, H.-I. Zhao, X.-t. Chen, and C.-I. Luo, *J. Mountain Sci.* **17**, 2982 (2020).
- [33] N. H. T. Nguyen, H. H. Bui, and G. D. Nguyen, *Granul. Matter* **22**, 59 (2020).
- [34] X. Su, X. Xia, Q. Liang, and J. Hou, *Comput. Geotech.* **141**, 104537 (2022).
- [35] T. Man, H. E. Huppert, L. Li, and S. A. Galindo-Torres, *Geophys. Res. Lett.* **48**, e2021GL096054 (2021).
- [36] T. Man, H. E. Huppert, L. Li, and S. A. Galindo-Torres, *Granular Matter* **23**, 59 (2021).
- [37] Z. Lai, D. Chen, E. Jiang, L. Zhao, L. E. Vallejo, and W. Zhou, *AIP Adv.* **11**, 095113 (2021).
- [38] L. Brezzi, F. Gabrieli, and S. Cola, *Acta Geotech.* **15**, 695 (2018).
- [39] A. C. Santomaso, S. Volpato, and F. Gabrieli, *Phys. Fluids* **30**, 063301 (2018).
- [40] A. Abramian, L. Staron, and P.-Y. Lagrée, *J. Rheol.* **64**, 1227 (2020).
- [41] P. Li, D. Wang, Y. Wu, and Z. Niu, *Powder Technol.* **393**, 357 (2021).
- [42] V. Richefeu, F. Radjai, and M. S. E. Youssoufi, *Eur. Phys. J. E* **21**, 359 (2007).
- [43] F. Gabrieli, R. Artoni, A. Santomaso, and S. Cola, *Phys. Fluids* **25**, 103303 (2013).
- [44] G. Wang, A. Riaz, and B. Balachandran, *Acta Geotech.* **15**, 1205 (2019).
- [45] A. Abramian, P.-Y. Lagrée, and L. Staron, *Soft Matter* **17**, 10723 (2021).
- [46] V. Topin, Y. Monerie, F. Perales, and F. Radjai, *Phys. Rev. Lett.* **109**, 188001 (2012).
- [47] C. Wang, Y. Wang, C. Peng, and X. Meng, *Phys. Fluids* **29**, 103307 (2017).
- [48] A. Bougouin and L. Lacaze, *Phys. Rev. Fluids* **3**, 064305 (2018).
- [49] C.-H. Lee, Z. Huang, and M.-L. Yu, *Phys. Fluids* **30**, 123307 (2018).
- [50] G. Pinzon and M. Cabrera, *Phys. Fluids* **31**, 086603 (2019).
- [51] A. Bougouin, L. Lacaze, and T. Bonometti, *Phys. Rev. Fluids* **4**, 124306 (2019).
- [52] L. Jing, G. Yang, C. Kwok, and Y. Sobral, *Powder Technol.* **345**, 532 (2019).
- [53] G. C. Yang, L. Jing, C. Y. Kwok, and Y. D. Sobral, *J. Geophys. Res.* **125**, e2019JF005044 (2020).
- [54] H. Liang, S. He, Z. Chen, and W. Liu, *Eng. Geol.* **260**, 105219 (2019).
- [55] L. Jing, G. C. Yang, C. Y. Kwok, and Y. D. Sobral, *Phys. Rev. E* **98**, 042901 (2018).
- [56] F. Ceccato, A. Leonardi, V. Girardi, P. Simonini, and M. Pirulli, *Soils Found.* **60**, 683 (2020).
- [57] A. M. Taylor-Noonan, G. A. Siemens, M. A. Cabrera, N. M. Arpin, F. Parera Morales, and W. A. Take, *Phys. Fluids* **33**, 033309 (2021).
- [58] G. Lefebvre and P. Jop, *Phys. Rev. E* **88**, 032205 (2013).
- [59] T.-T. Vo, P. Mutabaruka, S. Nezamabadi, J.-Y. Delenne, and F. Radjai, *Phys. Rev. E* **101**, 032906 (2020).
- [60] T.-T. Vo, C. T. Nguyen, T.-K. Nguyen, V. M. Nguyen, and T. L. Vu, *Comput. Particle Mech.* **9**, 537 (2021).
- [61] P. Li, D. Wang, and Z. Niu, *Phys. Rev. Fluids* **7**, 084302 (2022).
- [62] Y. Wu, Y. Sun, and D. Wang, *Soft Matter* (unpublished).
- [63] P. A. Cundall and O. D. L. Strack, *Géotechnique* **29**, 47 (1979).
- [64] F. Radjai and F. Dubois, *Discrete-Element Modeling of Granular Materials* (Wiley-Iste, New York, 2011).
- [65] S. Luding, in *Physics of Dry Granular Media*, edited by H. J. Herrmann, J.-P. Hovi, and S. Luding NATO ASI Series, E350 (Kluwer, Dordrecht, 1998), p. 285.
- [66] G. Lian, C. Thornton, and M. Adams, *J. Colloid Interface Sci.* **161**, 138 (1993).
- [67] M. Scheel, R. Seemann, M. Brinkmann, M. D. Michiel, A. Sheppard, and S. Herminghaus, *J. Phys.: Condens. Matter* **20**, 494236 (2008).
- [68] T.-T. Vo and T.-K. Nguyen, *Acta Geotech.* **18**, 217 (2022).
- [69] V. Richefeu, Moulay Said El Youssoufi, and F. Radjai, *Phys. Rev. E* **73**, 051304 (2006).
- [70] S. Herminghaus, *Adv. Phys.* **54**, 221 (2005).
- [71] T.-T. Vo and T.-K. Nguyen, *Comput. Particle Mech.* **10**, 1977 (2023).
- [72] R. Artoni, A. C. Santomaso, F. Gabrieli, D. Tono, and S. Cola, *Phys. Rev. E* **87**, 032205 (2013).
- [73] R. Greve and K. Hutter, *Philos. Trans. R. Soc. London A* **342**, 573 (1993).
- [74] K. Hutter, T. Koch, C. Plüß, and S. B. Savage, *Acta Mech.* **109**, 127 (1995).